Chapter 9
Fabrication of 3D Quantum Dot Array by Fusion of Bio-Template and Neutral Beam Etching I: Basic Technologies

Seiji Samukawa

Abstract The direct formation of a uniform, closely packed, and high density two-dimensional array of ferritin molecules is realized on Si and GaAs substrates using our developed neutral beam oxidation (NBO) technique to prepare the surface oxide. The NBO process is applied to form thin films by slight surface oxidations, which have negative zeta potential and highly hydrophilic surfaces. It is experimentally proven that surface hydrophilicity is essential for the mechanism of uniform and high density ferritin arrangement. Uniform and defect-free 2D and 3D array of Si-NDs with ND density of more than 7×10^{11} cm^{-2} were realized as Si-QDSLs using combination of bio-templates and NBE processes. The diameter of Si-ND can be controlled by changing the conditions under which surface-oxide removal was conducted. 2D array of GaAs-NDs with ND density of 7×10^{11} cm^{-2} has been also developed successfully. Each step of the process, i.e., ferritin protein shell removal, NBE, and iron core removal, has been investigated and several novel solutions have been developed that do not damage the GaAs substrate. O-radicals are first found to eliminate the protein shell effectively at a low temperature of 280 °C without deteriorating surface roughness or moving the iron oxide cores. NBE with a 22 % chlorine and 78 % argon gas mixture and 16 W RF bias power can etch a GaAs nanostructure with a diameter of about 10 nm, atomic-level surface roughness of less than 1 nm and vertical taper angle of 88°.

Keywords Bio-template · Neutral beam etching · 2D array of ferritin molecular · Nanodisk

S. Samukawa (✉)
Institute of Fluid Science, Tohoku University, Sendai 980-8577, Japan
e-mail: samukawa@ifs.tohoku.ac.jp

J. Sone and S. Tsuji (eds.), *Intelligent Nanosystems for Energy, Information and Biological Technologies*, DOI 10.1007/978-4-431-56429-4_9

9.1 Introduction

As material size shrinks to a nanometer scale, the materials start to show specific electrical and optical characteristics based on the quantum confinement of conduction band electrons, valence band holes or excitons in several nanoscales. Recently, super lattices with closely packed quantum dots (QDSLs) with high-uniformity, and high density have been received great attention to develop high-performance optoelectronic devices, including lasers and solar cells. Bandgap energy (E_g) of the QDs is engineered by adjusting the size of the QDs [1–4]. In super lattices with close-packed and well-aligned QDs, wave functions of QDs overlap each another, and discrete energy levels of each QD merge to form broadened mini-bands [5–9]. For photovoltaic applications, such engineered QDs can be used as an adjustable absorber layers with intermediate bandgap energy and applied to tandem solar cells [9–12]. Highly efficient solar cells is expected using SiC as interlayer material instead of SiO_2 and SiN, because carrier wave function easily spreads into the interlayers due to its lower bandgap energy. Quantum dot (QD) of III–V compounds has also been formed by bottom-up process such as Stranski–Krastanov growth based on self-organization [13] and attractive to develop optoelectronic devices including high-performance QD lasers [1–4]. In this method, there is some limitation in forming QDs with high density and separation enough to avoid the coupling of wave functions to realize high gain laser. However, it is difficult to fabricate defect-free nanostructures using conventional top-down process technologies such as epitaxy followed by photolithography, plasma etching, co-sputtering, and annealing [14–17].

In this chapter, to break-through the above problems, our innovative processes for fabrication of uniform and closely packed arrays of sub-10-nm Si and GaAs nanodisks (GaAs-ND) was realized using a damage-free neutral beam (NB) etching technology combined with a bio-template process to address these issues.

9.2 Top-Down Process for the Fabrication of Sub-10-nm Structure

To address the problems in the process technologies discussed above, we proposed a new fabrication method of uniform and closely packed arrays of sub-10-nm Si and GaAs nanodisks (GaAs-ND) which combines a bio-template [18] and damage-free neutral beam etching [19]. We employ ferritins to make a nano-etching mask. The ferritins produced from DNA information can make uniform 7-nm iron oxide (Fe_2O_3) cores in their cavities. A high density 2D-ordered array of ferritin on a substrate provides an array of independent cores with distances that are roughly twice the protein shell thickness after selective protein shell elimination. By using the iron core as an etching mask, our developed neutral beam etching processes could fabricate 2D array of defect free nanodisk on any kind of materials.

9.2.1 Neutral Beam Sources for Damage-Free Etching and Surface Oxidation

For the development of damage-free etching processes, neutral beam (NB) sources have been investigated as substitutes for conventional plasma source. Using the sources, damage-free etching processes can be achieved by eliminating charged particles (ions and electrons). During etching, energetic neutral beams, rather than ions, bombard the wafer surface where radicals absorb, resulting in the removal of the materials. In particular, Samukawa has developed practical NB sources for high-performance neutral beam etching. Figure 9.1 provides a schematic representation of a NB source that consists of an ICP and parallel carbon plates [19–21]. The process chamber is separated from the plasma chamber by a bottom electrode made of carbon, which has the low sputtering yield under high-energy bombardment and does not contaminate semiconductor devices. Neutral beams are extracted from the plasma through numerous high-aspect-ratio apertures in the bottom electrode. The NB sources employ pulse-time-modulated ICPs to generate large quantities of negative ions, which are more effectively neutralized than positive ions because the detachment energy of electrons from negative ions is much smaller than the charge transfer energy of positive ions. In previous-generation neutral beam sources, where neutral beams are obtained through the charge transfer of positive ions, the neutralization efficiency is at most 60 % and the beam energy must be greater than 100 eV to obtain a large degree of neutralization of positive ions. On the other hand, a NB source using Cl_2 plasma with pulsed operation can obtain a neutralization efficiency of almost 100 % and high neutral beam flux of more than 1 mA/cm^2. At the same time, because of the presence of apertures, UV radiation

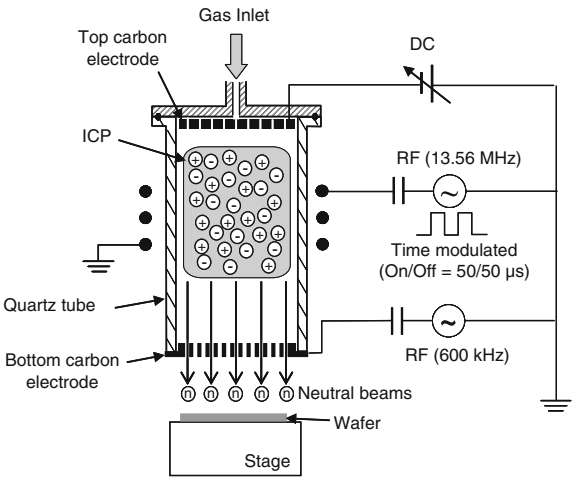

Fig. 9.1 Schematics of neutral beam system

from the plasma is shaded and/or absorbed in the bottom electrode; consequently, UV radiation damage can be eliminated. The NB process is a promising solution for next-generation nanoscale device fabrication, which requires damage-free etching conditions [19–25]. Additionally, we also developed damage-free neutral beam oxidation (NBO) for the fabrication of ultrathin oxide films on Si and GaAs surfaces at a temperature of less than 300 °C using energy-controlled oxygen neutral beam [22–24]. In this system, the Si aperture was used for neutral beam generation to eliminate carbon contamination at the interface.

9.2.2 High Density Ferritin Arrangement

A uniform, closely packed, and high density 2D array of ferritin molecules was directly formed on a Si and GaAs substrate with preparation of surface oxide. The NBO process [22–25] was applied to form both SiO_2 and GaAs oxide thin films that have negative zeta potential and highly hydrophilic surfaces [26, 27]. To form the high density 2-dimensional ferritin array, two interactions should be considered, i.e., ferritin–ferritin and ferritin–substrate interaction. The former interaction is an attractive force due to the hydrophobic interaction between ferritins derived from the carbonaceous binding peptides [28, 29]. Therefore, the interaction between ferritin and surface plays an important role in this study. When the ferritin solution is dropped onto a hydrophilic surface, ferritin molecules spread over the substrate and are then absorbed onto the surface oxide [28]. When the surface oxide is highly hydrophilic, such as with Si-NBO or GaAs-NBO, the surface hydrophilicity would reduce the absorption force of the ferritin, as shown in Fig. 9.2. A negative zeta potential would also weaken the interaction between the ferritin and NBO surfaces. Therefore, soft absorption between ferritin molecules and the oxide surface was realized, and the ferritin could attain sufficient degree-of-freedom of movement and then easily reform the arrangement to make a closely packed array. In other words, absorption force between ferritin and substrate was weak enough to allow ferritins to be rearranged by attractive protein–protein interaction. A repulsive force due to the negative charge of ferritin and the negative potential of the oxide surface may also help prevent multilayer generation of ferritins on the substrate. On the other hand, if the absorption force is stronger in the case of using thermal oxide (TO), ferritin will not move again once it absorbs to the surface, which results in a disordered arrangement. This might be what happened with the TO. The reason the adsorption force is strong with TO is not clear, but the difference in hydrophilicity might explain it. There might be an attractive force between the hydrophobic surface patches of ferritin and the TO substrate. To prove this hypothesis, we need to conduct more studies on ferritin adsorption behavior.

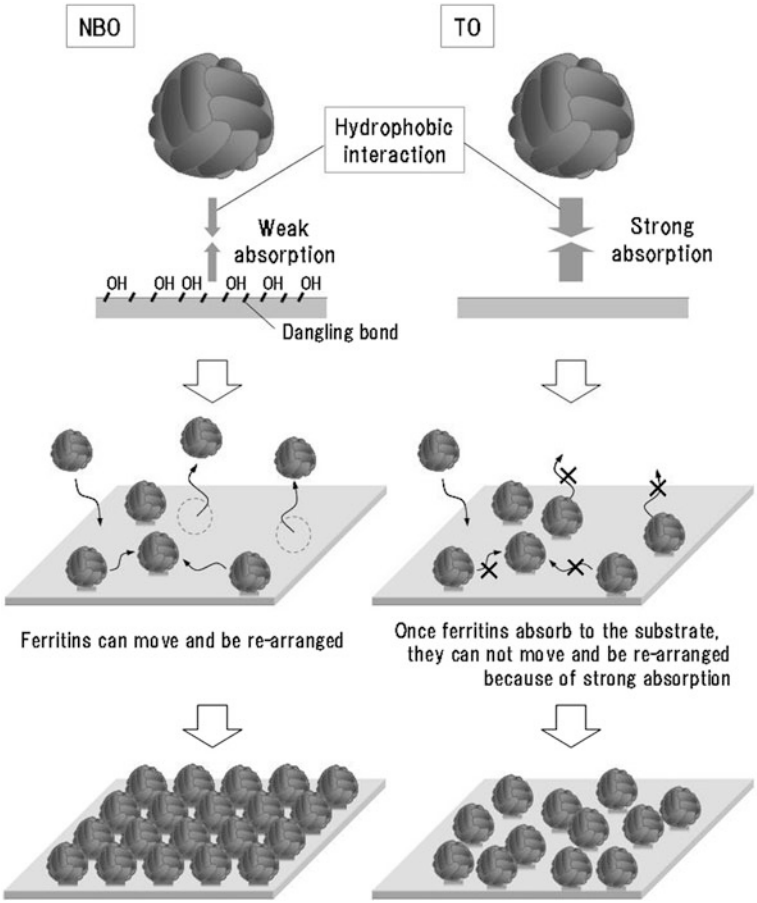

Fig. 9.2 Schematic image of uniform and high density arrangement mechanism [23]

9.3 Fabrication of Silicon Nanodisks

9.3.1 Process Flow

To measure optical transmittances, we prepared 2D arrays of Si-NDs with SiO_2 or SiC matrix on quartz substrate. The fabrication of a 2D Si-ND array structure using the two types of bio-template of ferritin and Listeria-Dps (Lis-Dps) and damage-free NB etching is schematically shown in Fig. 9.3a–i. The fabrication steps are as follows. First, 2–12 nm-thick poly-Si and 3-nm-thick Si-NBO (SiO_2) layers were fabricated on a 10 × 10 mm^2 quartz substrate as shown in Fig. 9.3b, c. The poly-Si

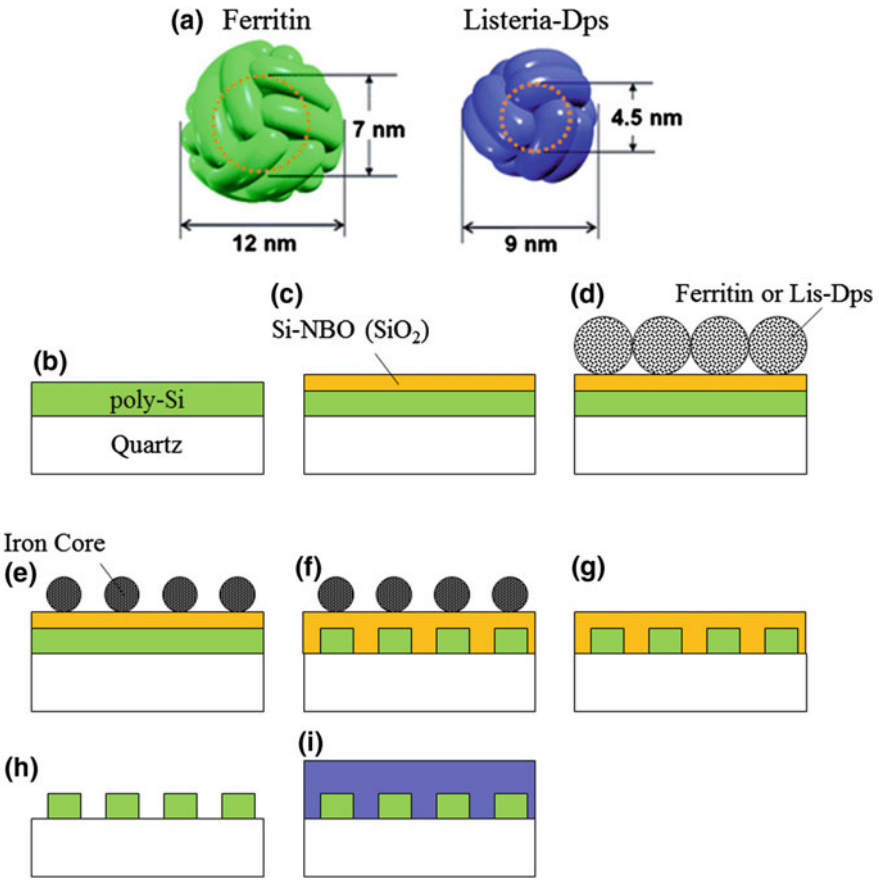

Fig. 9.3 Flow of sample preparation

layer was prepared using molecular beam epitaxy with a controlled deposition rate of 0.05 nm/min followed by annealing in argon atmosphere at 600 °C for 16 h. By in situ monitoring the poly-Si deposition thickness we could precisely control the thickness of the Si-ND. Then a 3 nm SiO_2 layer was fabricated using our developed neutral beam oxidation process at a low temperature of 300 °C as a surface oxide (Si-NBO) [22–24]. Second, a new bio-template of a 2D array of ferritin (a 7.0 nm diameter iron oxide core in the cavity) or Lis-Dps (a 4.5 nm diameter iron oxide core) molecules was formed as shown in Fig. 9.3d. Lis-Dps is a Dps protein that is synthesized from Listeria bacteria. It has a spherical protein shell with an external diameter of 9.0 nm and a cavity diameter of 4.5 nm, and biomineralizes iron as a hydrate iron oxide core (diameter: 4.5 nm) in the cavity and stores it. Using iron oxide core as the 4.5 nm diameter etching mask, we would like to realize a much smaller diameter size of the Si-ND structure. Next, protein shells were removed by heat treatment in oxygen atmosphere at 500 °C for 1 h to obtain a 2D array of iron

oxide cores as the etching masks, as shown in Fig. 9.3e. Etching was carried out by combination between NF_3/H-radicals treatment at 100 °C [30, 31], and anisotropic etching of poly-Si using Cl_2 NB, respectively, as shown in Fig. 9.3f [23]. During the etching process by changing the NF_3/H-radicals treatment time to 15 and 40 min we could change the diameter of ND due to the side etching of Si-NBO. Then, the 2D iron oxide core array was removed using hydrochloric solution to obtain a 2D Si-ND array structure, as shown in Fig. 9.3g. Because the native oxide grows between Si-NDs, we call this structure simply a 'Si-ND array structure with a SiO_2 matrix.' For fabrication of the Si-NDs with SiC matrix, finally, the SiO_2 matrix was removed by the NF_3/H-radicals treatment and then a 3-nm-thick SiC was deposited on Si-NDs by sputtering system as shown in Fig. 9.3h, i.

Figures 9.4a and 9.5a show a top-view SEM image of the 2D Si-ND array structure fabricated using Ferritin and Lis-Dps as the etching mask, which consisted of a closely packed array of 7 and 4.5 nm diameter iron oxide cores on the Si-NBO surface. As the figure shows, this array structure had a high density (7×10^{11} and 1.4×10^{12} cm^{-2} respectively), uniform size (Si-ND diameter: 6.4 and 10 nm) and well-ordered arrangement (quasi-hexagonal ordered arrays). The density of the 2D Si-ND array structure fabricated using Lis-Dps increased to two times that of the array fabricated using ferritin, while the diameter of the Si-ND shrunk to 61 % of that obtained using ferritin with 40 min NF_3/H-radicals treatment. To confirm regularity in this array, we measured the center-to-center distance between adjacent Si-NDs, as shown in the SEM image in Figs. 9.4b and 9.5b. These figures show that the standard deviation of the center-to-center distance was less than 10 %. The results show that the 2D Si-ND array structure fabricated using a Ferritin and Lis-Dps etching mask with a 4.5 and 7 nm diameter iron oxide core formed a 2D superlattice structure with a highly density and well-ordered arrangement, making it a suitable quantum dot structure.

9.4 Photoluminescence in Silicon Nanodisk

To analyze defects at the interface between a Si-ND and the SiO_2 matrix, high-sensitivity electron spin resonance (ESR) analysis was performed to quantify the presence of any paramagnetic defects. We used Si-NBO grown onto a p-type Si wafer with a (111) surface orientation and a high resistivity of more than 1000 Ω cm. ESR measurement was performed on the samples at 4 K using a Bruker-ESP300E spectrometer. The microwave frequency and power were approximately 9.62 GHz and 0.1 mW, respectively. The paramagnetic (P_b) center density at the Si-ND/Si-NBO (SiO_2) interface was 5.0×10^{10} cm^{-2}. Incidentally, the surface areas of the (7 nm in diameter) Si-NDs with thicknesses of 4 and 8 nm were 1.6×10^{-12} and 2.5×10^{-11} cm^2, respectively. Therefore, we were able to estimate the number of defects in 4 and 8 nm-thick Si-NDs at 0.08 and 0.16, respectively. In achieving these results, we found that the interface between the Si-NDs and the SiO_2 matrix was almost completely defect-free.

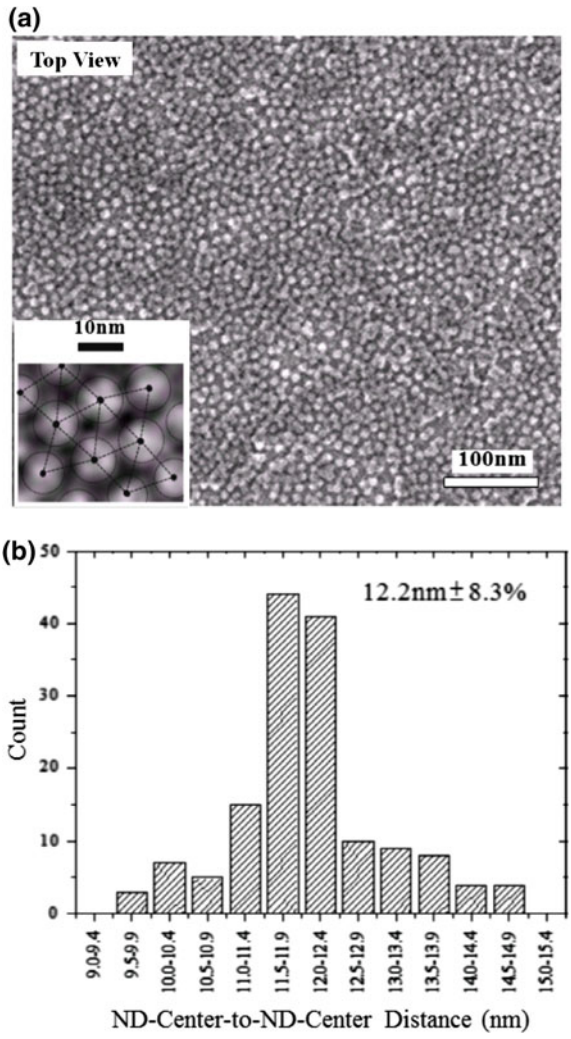

Fig. 9.4 **a** SEM picture of 2D array of Si-NDs. **b** Distribution of ND-Center-to-ND-Center distances

Silicon is basically an indirect band gap semiconductor and thus its optical absorption and radiative recombination efficiencies are markedly low. On the other hand, with a QD structure, the surface effect and size effect, which modify the carrier wave function, can improve radiative recombination efficiency [32–34]. However, in the conventional fabrication processes, a large amount of defect-induced and interfacial local energy levels can be formed easily. As a result, the majority of experiments on Si nanostructures have shown extremely slow decaying PL with decay times ranging from several tens of nanoseconds to microseconds. This can be attributed to carriers recombining at the defect states rather than the nanostructure itself [33]. With this in mind, we researched photo-excited emissions from the Si-ND array structure. Figure 9.6 shows time-integrated PL spectra of a 2D array of 8-nm-thick Si-NDs with

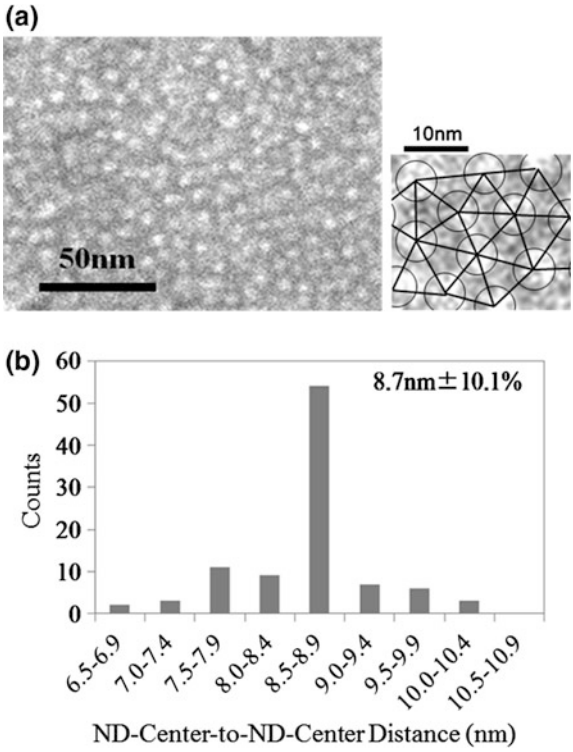

Fig. 9.5 **a** SEM image of 2D Si-NDs array using Lis-Dps. **b** Distribution of ND-center-to-ND-center distances

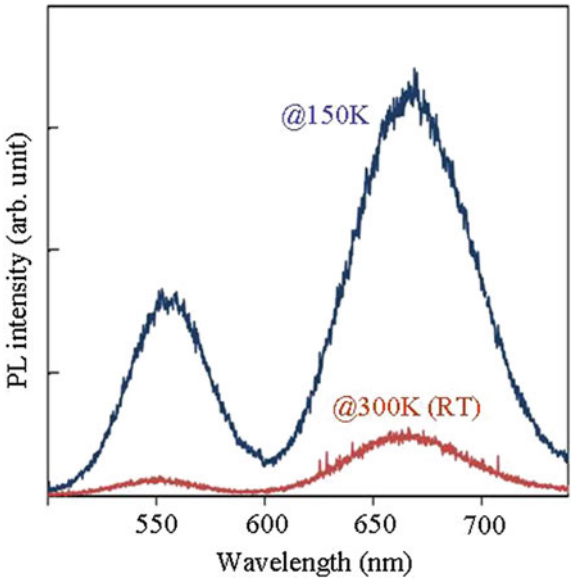

Fig. 9.6 Time-integrated PL spectra of a 2D array of 8-nm-thick Si-NDs with a SiO_2 interlayer for an excitation power of 50 mW

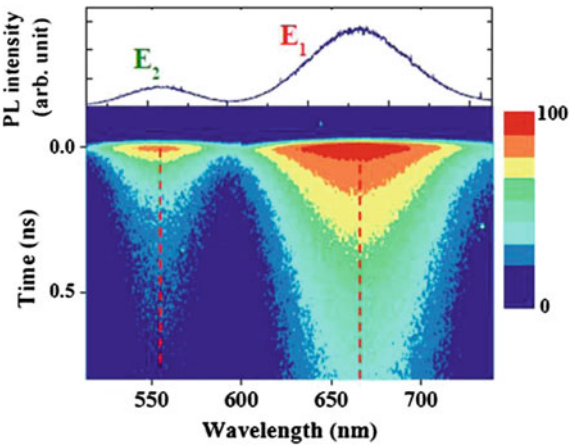

Fig. 9.7 Time-integrated and time-resolved PL spectra of a 2D array of 8-nm-thick Si-NDs measured at a temperature of 150 K

a SiO_2 interlayer for an excitation power of 50 mW. We performed the measurement from 10 to 300 K. The result shows two PL emissions centered at wavelengths of 665 nm (E_1: 1.86 eV) and 555 nm (E_2: 2.23 eV), and the highest peak of PL intensity was observed at 150 K. Moreover, PL emission of 2D array of Si-NDs structure also could be observed even in the room temperature. Figure 9.7 shows time-integrated and time-resolved PL spectra of a 2D array of 8-nm-thick Si-NDs measured at a temperature of 150 K. While the decay characteristic of two PL bands is slow in the case of conventional self-assembled QD, i.e., the microsecond region originating in local states in Si and SiO_2 induced by a defect or interface state [33], both peaks in our structure show short lifetimes of 3 ns or less. Therefore, we can rule out assigning the emission bands to defect-related emissions.

9.5 Control of Bandgap Energy by Geometric Parameters of Nanodisk

Figure 9.8a shows the results of E_g as a function of Si-ND thickness. We found that, for the 2D array of Si-NDs, E_g can be controlled from 2.3 to 1.3 eV when the ND thickness is changed from 2 to 12 nm. We also saw that, when the poly-Si thin film thickness changes from 2 to 8 nm, E_g varies from 1.6 to 1.1 eV, which is the E_g of bulk Si. From these results, as shown in Fig. 9.8a, we know that the controllable E_g range of a 2D array of Si-NDs is much larger than that of poly-Si thin film. Figure 9.8b shows the results of E_g as a function of Si-ND diameter controlled by the bio-templates and NF_3/H-radicals treatment. By shrinking the Si-ND diameter from 12.5 to 6.4 nm, the E_g increased from 1.9 to 2.1 eV even at a ND thickness of 4 nm. We found that the E_g could be controlled by both Si-ND thickness and diameter. The diameter from 6.4 to 12.5 nm allowed the E_g to be changed in the range of 0.1 eV, while controlling the thickness from 2 to 12 nm

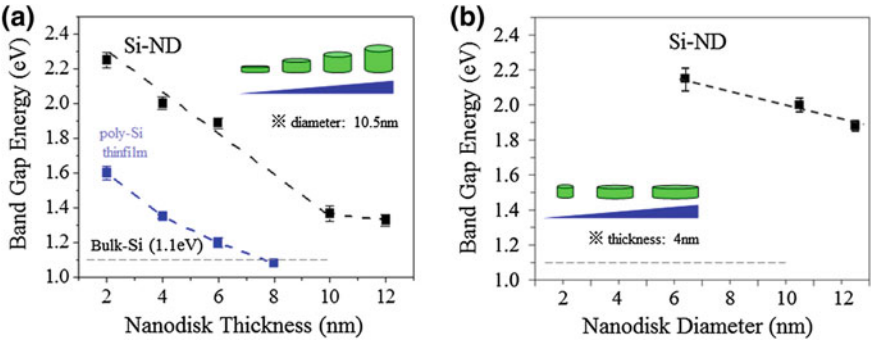

Fig. 9.8 Bandgap control by changing thickness and diameter

allowed the gap to change in the range of 0.5 eV. This result also suggests that stronger quantum confinement occurs in the thickness direction. These results made it clear that independently changing the geometric parameters of thickness and diameter in our proposed Si-ND array structure enables the optical band gap energy to be precisely designed within a wide range. This wide controllable range of E_g is very suitable for developing all-Si tandem solar cells. For the three cells of all-Si tandem solar cells, the E_g of the top and middle cells requires 2.0 and 1.5 eV, respectively [35].

9.6 Fabrication of Gallium Arsenide Nanodisks

9.6.1 Process Flow

The process flowchart is shown in Fig. 9.9 and described next. (1) The GaAd substrate was sequentially cleaned using acetone, ethanol, and deionized water for 5 min, respectively, in an ultrasonic bath (Fig. 9.9a). (2) The surface native oxide of GaAs was removed through a hydrogen-radical treatment at 280 °C with a hydrogen flow rate of 40 sccm, process pressure of 40 Pa, and 2.45 GHz microwave power of 200 W (Fig. 9.9b). (3) After native oxide removal, the GaAs substrate was transferred to a neutral beam oxidation (NBO) chamber in a vacuum environment and then sequentially oxidized to form a 1-nm-thick GaAs–NBO film at room temperature with an O_2 flow rate of 5 sccm, process pressure of 0.14 Pa and 13.56 MHz RF power of 500 W (Fig. 9.9c). (4) Ferritin molecules were spin-coated on the GaAs-NBO surface for 500 rpm in 2 s and 3000 rpm in 30 s to form the 2D array monolayer (Fig. 9.9d). (5) The protein shell of the ferritin was removed through an O-radicals treatment with a temperature of 280 °C, O_2 flow rate of 30 sccm, process pressure of 50 Pa and 2.45 GHz microwave power of 200 W (Fig. 9.9e). (6) After removal of the ferritin protein shell, the iron oxide cores inside the ferritin remain as the etching mask and then GaAs was etched by a

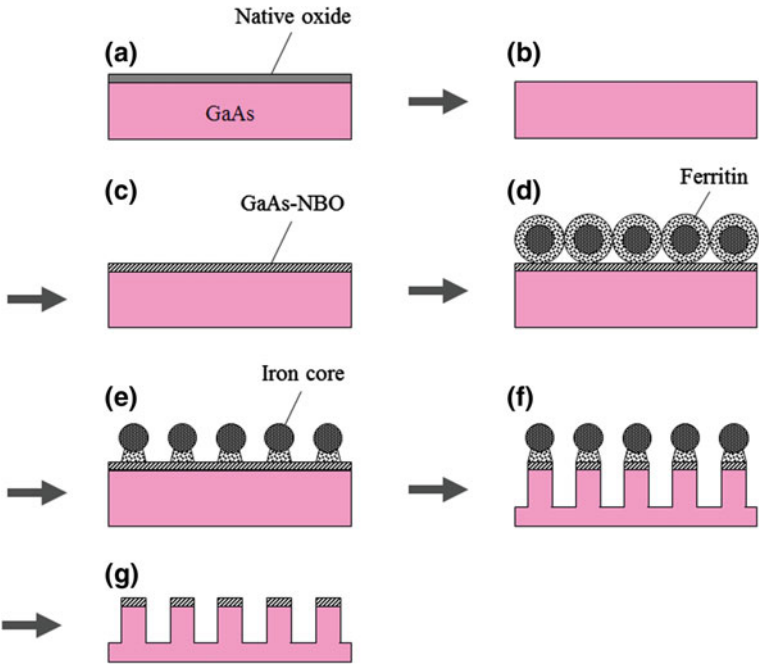

Fig. 9.9 Process flow for fabricating 2D array of GaAs-QDs

neutral beam process (Fig. 9.9f). (7) Finally, the iron oxide cores were removed using a diluted hydrogen chloride solution (HCl:H_2O = 1:10), resulting in the 2D array of GaAs-QDs (Fig. 9.9g).

There are two conventional approaches to removing the ferritin protein shell: ultraviolet (UV) ozone treatment at 150 °C and oxygen annealing at a high temperature of 500 °C. The UV ozone treatment produces UV irradiation damage that would seriously damage the GaAs QD crystalline structure, and the high temperature oxygen annealing would cause severe surface roughness because of desorption of As. Therefore, a low temperature process without UV light needs to be developed for removing the ferritin protein shell. In this work, we first developed an O-radicals treatment approach to removing the ferritin protein shell. The O-radicals system consists of a plasma chamber and treatment chamber that are connected by a φ2 mm aperture (Fig. 9.10). The O-radicals are extracted from plasma generated by a 2.45 GHz RF power source and are passed through the aperture into the treatment chamber. Meanwhile, the UV light from the plasma would be eliminated by the φ2 mm aperture.

In this condition, we found that 280 °C O-radicals treatment was confirmed to remove protein shells effectively. Then, top-view SEM images were observed to check whether the iron oxide cores were still arranged as well as before the treatment. Three different treatment times were investigated: 30, 45, and 60 min.

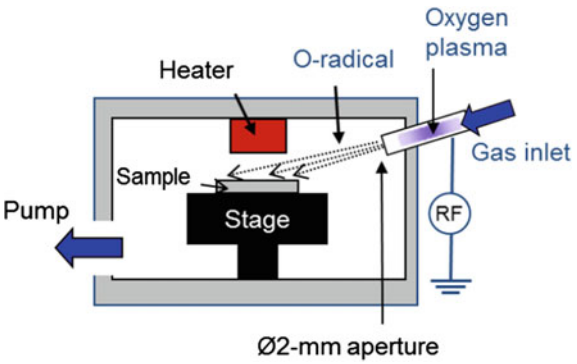

Fig. 9.10 Illustration of O-radicals system

After the 30 min treatment, in a comparison with the SEM image of 2D array ferritins, the iron oxide cores were still arranged in order of high density, as shown in Fig. 9.11a. However, after the 45 min treatment, part of the iron oxide cores moved and some locations were not occupied by iron cores (Fig. 9.11b). Furthermore, after the 60 min treatment, many of the iron cores not only moved but also aggregated together (Fig. 9.11c)

Initially, the O-radicals only contact and react with the upper parts of the protein shell. As treatment time increases, most of the upper part of the protein shell would be removed while the bottom part still exists. The iron core would be exposed

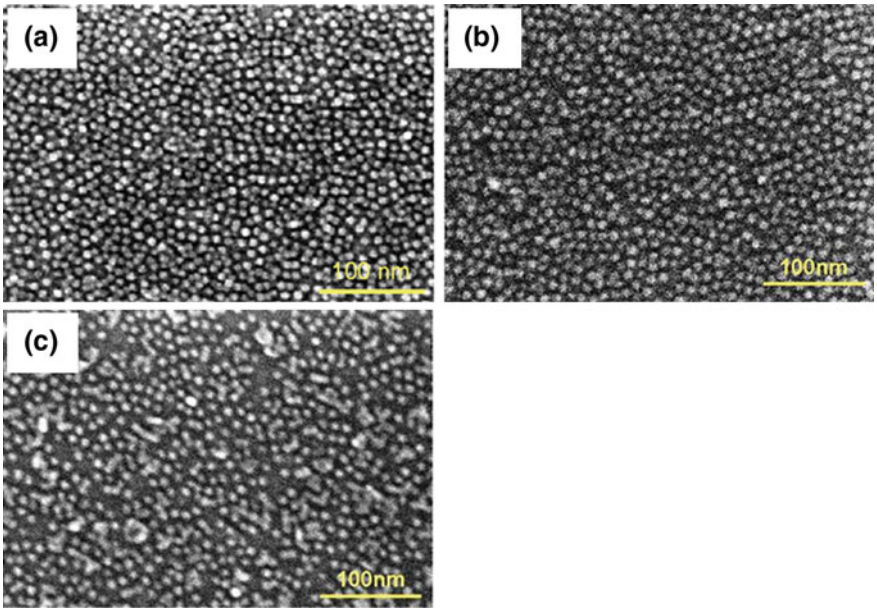

Fig. 9.11 Top-view SEM images after 280 °C O-radicals treatment with different treatment time: **a** 30 min, **b** 45 min, and **c** 60 min

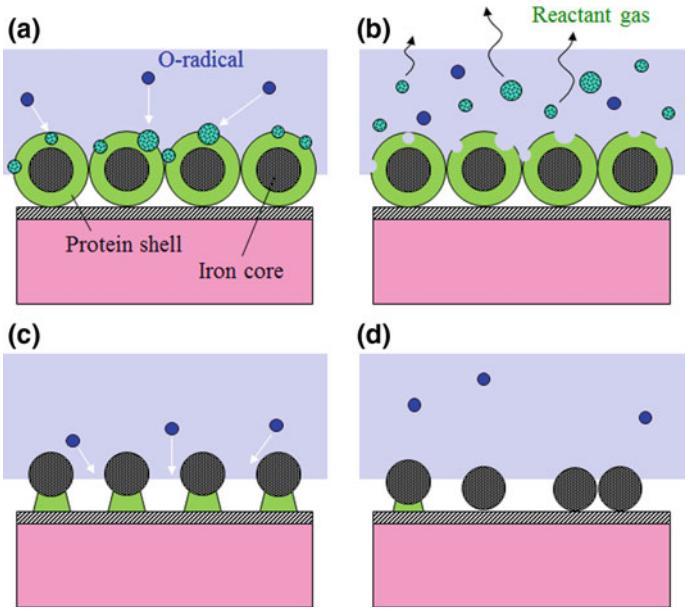

Fig. 9.12 Schematic of ferritin protein shell removal with oxygen-radical treatment at 280 °C (from **a** to **d**)

without moving because it is supported by the residual protein shell (Fig. 9.12c). This situation is similar to the experiment results after the 30 min O-radicals treatment at 280 °C (Fig. 9.11a). However, when the treatment time is longer than 30 min, the bottom part of the protein shell would also be eliminated by the O-radicals. Finally, the iron oxide core loses all protein shell support and thus moves easily (Fig. 9.12d), as in the experimental results of the 45 min (Fig. 9.11b) and 60 min (Fig. 9.11c) treatments. To summarize and to maintain the arrangement of a 2D array iron core, a suitable treatment time at 280 °C is necessary. Although FTIR analysis cannot detect the C=O and N–H bond signals of ferritin protein after treatment for 30 min at 280 °C, it is believed that the small bottom parts of the residual protein, which fixed the iron oxide cores in order as shown in Fig. 9.9e, were very few and cannot be detected. In this work, the O-radicals treatment for 30 min at 280 °C can remove the ferritin protein shell without changing the arrangement of a high density 2D array of iron oxide cores.

9.6.2 GaAs Nanostructure Etching by Neutral Beam

After O-radicals treatment, an atomic-level smooth surface with well-arranged iron oxide cores can be obtained for the etching process. The next step is to investigate the etching conditions of the neutral beam process. Quantifying the cross-sectional

etching profile of single GaAs nanostructures inside the 2D array is very difficult by SEM or transmission electron microscopy because the high in-plane density of the GaAs-NDs array causes an indistinct background. Therefore, we tried to reduce the density of the GaAs-NDs by diluting a ferritin solution by 400 times with deionized water. Following the process steps from Fig. 9.9a–d, the diluted ferritin solution can be spin-coated on the GaAs-NBO surface and arranged randomly with a low in-plane density.

In GaAs etching, the gallium and arsenic components have different chemical reactions during the etching process. Their different reaction rates would increase the etched surface roughness. Therefore, in previous work [36], we used chlorine and argon gas mixture as the reaction gas in the NBE process. The addition of an argon neutral beam (Ar-NB) can buffer the different chemical reaction rates of Ga-Cl and As-Cl from a chlorine neutral beam (Cl-NB). An atomic-level etched surface roughness can be obtained. In this work, the mixed gas ratio and 600 kHz RF bottom bias power were optimized for etching sub-10 nm GaAs nanodisk structure. The other process conditions of plasma source RF power, plasma RF time-modulated ratio, top electrode bias, and substrate temperature were fixed as 800 W, 50 μs ON/50 μs OFF (duty ratio: 50 %), 100 Vdc and −16 °C, respectively.

SEM images for samples etched by NB with different mixtures of gas and bias power are shown in Fig. 9.13. Etching results of pure chlorine gas and 6 W RF bias power are shown in Fig. 9.13a. The etched surface roughness was higher than

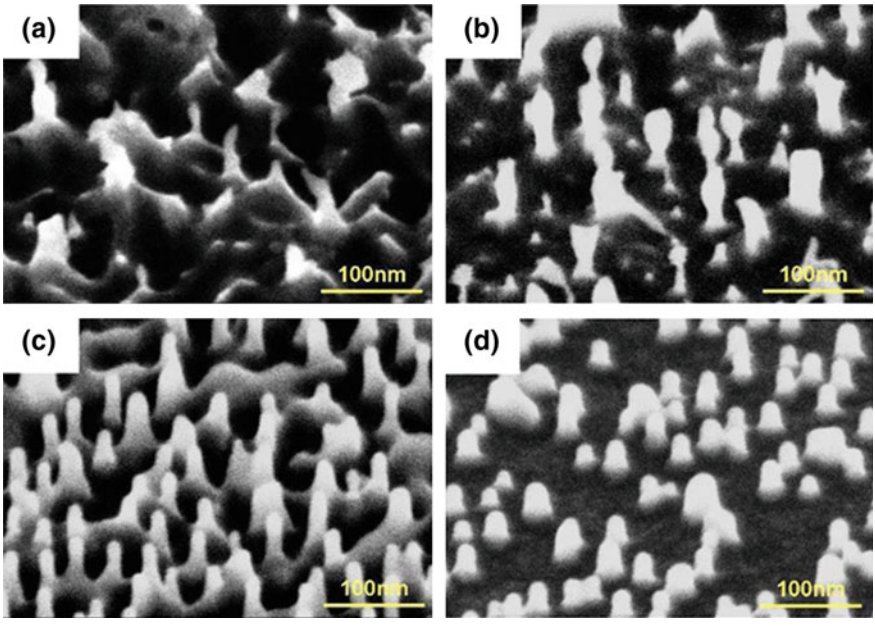

Fig. 9.13 SEM images with 40° tilt angle of neutral beam etched GaAs nanostructures with different gas and bias power conditions

20 nm and only a few GaAs nanocolumn structures remained distinct. These results show that a pure chemical reaction at low bias power not only causes serious surface roughness but also has a serious problem of undercut etching. The undercut etching would easily eliminate nanocolumns whose diameters were less than 10 nm. The results of pure chlorine gas again being used but RF bias power increased to 16 W are in Fig. 9.13b. More nanocolumn structures remained after etching and the surface roughness was improved, but the sidewalls of the nanocolumns were not vertical. These pure chlorine gas etching results indicate that the undercut etching and surface roughness problems happened at low bias power and for pure chemical etching. Pure chemical etching with low ion bombardment energy performs more like isotropic etching, which causes a serious undercut problem.

On the basis of these results and previous work [36, 37], a high argon mixed ratio was expected to reduce the etching surface roughness and buffer the chemical reaction from Cl-NB. Figure 9.13c shows a sample that was etched with a Cl_2: Ar = 22:78 (total flow rate was 40 sccm) gas mixture and 10 W RF bias power. The undercut etching problem was dramatically reduced, but the bottom surface roughness was still larger than 10 nm. The etching conditions of the sample shown in Fig. 9.13d were a 78 % Ar mixed ratio and 16 W RF bias power. The undercut phenomenon was eliminated and the bottom surface was smooth. In Fig. 9.13d, the SEM image was taken with a tilt angle of 20° and the electron charge problem was serious on the surface of the GaAs nanocolumns. Hence, the diameters of the nanocolumns seem larger than 10 nm. The cross-sectional SEM image was observed to investigate more precise dimensions, as shown in Fig. 9.14 [38–40]. The top diameters of the nanocolumns and etching depth were ∼10 and ∼45 nm, respectively. The taper angle of a nanocolumn was about 88°. In the results, the top diameter of a nanocolumn was a little larger than an iron oxide core's diameter of 7 nm. Since the flux of NB near the iron oxide core mask is lower than that in wide space without the iron core, the etching rate of GaAs oxide is lower than that of

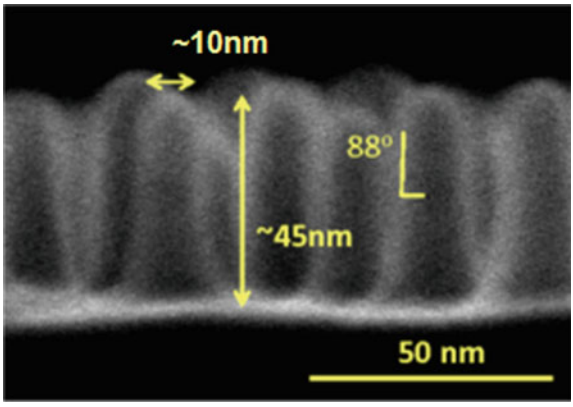

Fig. 9.14 Cross-sectional SEM images of GaAs-etched sample in Fig. 9.18d

GaAs. In the real etching process, a certain amount of GaAs was etched in the wide space before the GaAs oxide was completely etched near the iron oxide core mask. Therefore, a nanocolumn with a larger diameter was fabricated.

9.6.3 *Fabrication of High Density Dispersed GaAs Nanodisks with AlGaAs Matrix*

In this experiment, we used PEG ferritin (Fig. 9.15a) which was the ferritin modified with poly ethylene glycol (PEG) as the bio-template in order to realize large distance between ferritins. Considering laser devices, the coupling of wave-functions between GaAs-NDs should be avoided to confine carriers strongly into each QDs and enhance probability of radiative recombination. Figure 9.15b shows SEM images ferritin arrangement. Using PEG ferritin, a high density (more than 10^{11} cm^{-2}) and large distance (ferritin-to-ferritin distance is around 25 nm) PEG ferritin array were formed on the GaAs substrate [41].

Cross-section SEM profile of etched sample was shown in Fig. 9.16a. We could achieve the fabrication high-aspect ratio nanopillars which include GaAs nanodisks using a GaAs/AlGaAs structure. Further experiments revealed that the etching rates for GaAs and $Al_{0.3}GaAs$ bulk materials were 30 and 20 nm/min, respectively, which mean a low etching-selectivity (GaAs/AlGaAs) of 1.5. This low etching-selectivity resulted in a vertical and high-aspect ratio nano-pillar etching through the GaAs/AlGaAs structure without creating defects in the nanodisk structure [42]. Atomic-level transmission electron microscopy (TEM) picture was shown in Fig. 9.16b to further evaluate nanopillars crystal quality. We found that our nanopillars exhibit highly ordered and well-aligned atomic alignments at the etched side-wall, an ideal single-crystal structure; even none of any disordered atoms induced by defects were observed at the distinct and smooth interfaces. Theses result clarified that defect-free, atomically flat side-wall, and anisotropic GaAs etching have been achieved using our new processes.

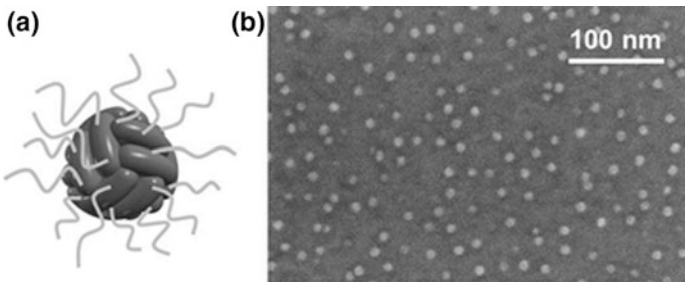

Fig. 9.15 **a** Illustration of PEG ferritin, **b** top-view SEM image of PEG ferritin arranged on GaAs substrate

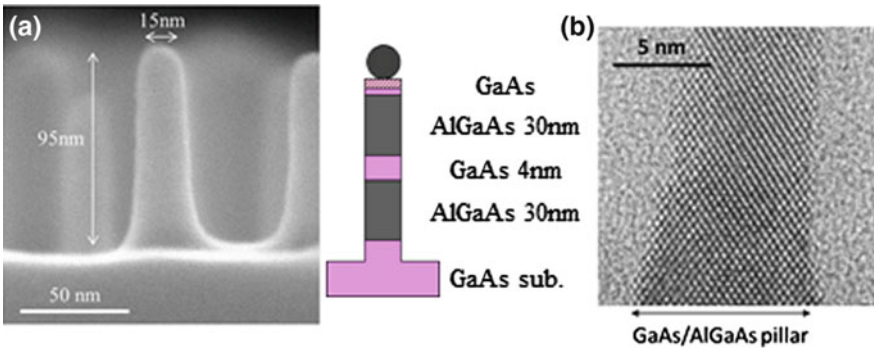

Fig. 9.16 **a** SEM image of GaAs/AlGaAs nanopillar including GaAs nanodisk, **b** TEM picture of nanopillar

9.7 Photoluminessence in Gallium Arsenide Nanodisks

Then, photoluminescence (PL) measurement was performed for the GaAs-NDs. Figure 9.17 shows the SEM images after NBE and GaAs regrowth. As we can see conformal capping layer were regrown on the pillars.

PL spectra were measured to evaluate exciton states and optical transitions in our GaAs-ND as shown in Fig. 9.18a; sample-A and B include GaAs nanodisks with the thickness of 4 and diameter of 15 nm, thickness of 4 and diameter of 10 nm, respectively. As the reference, we measured double-QW sample including two QW layers; 4 and 8 nm GaAs-QW.

Samples were excited by second harmonic light pulses from a mode-locked Ti: sapphire laser at a wavelength of 400 nm that provided ultrashort pulses with a time width of 150 fs and an excitation density of 0.3 μJ/cm^2. The time-resolved PL spectra were detected by a synchroscan streak camera. The time width of the

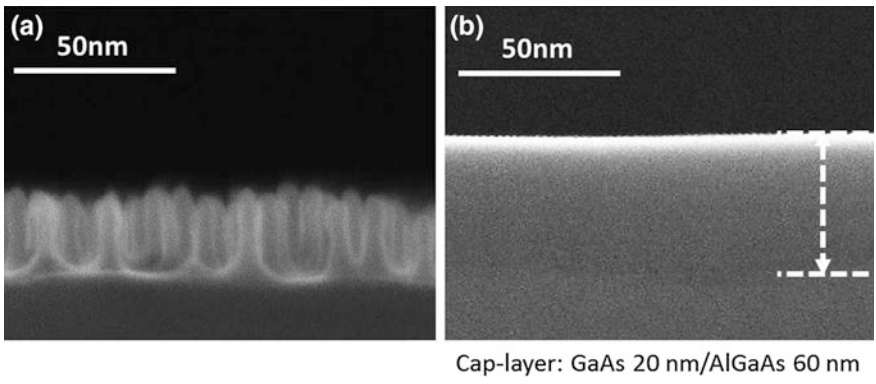

Fig. 9.17 Cross-section SEM images, **a** after neutral beam etching, **b** after regrowth

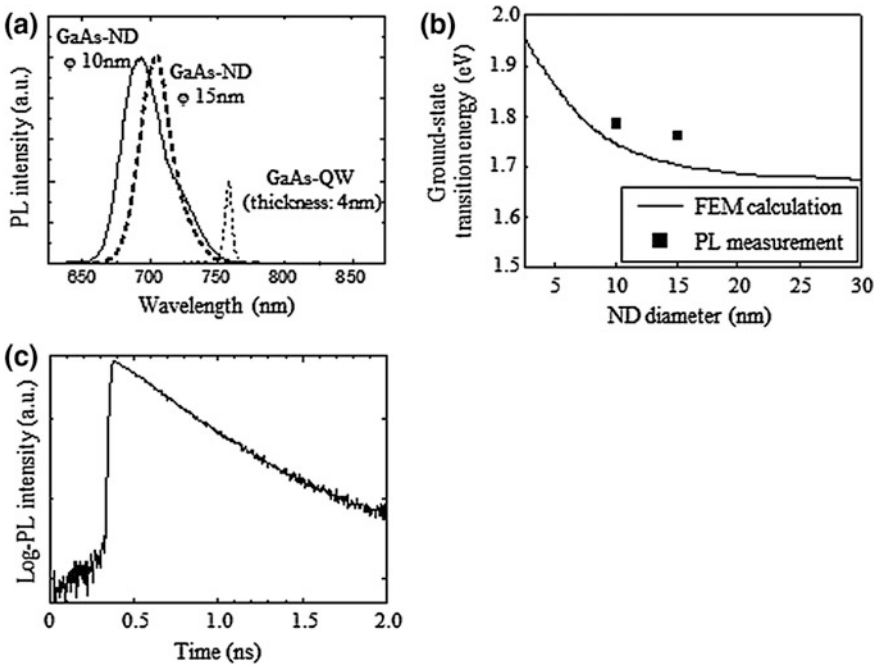

Fig. 9.18 **a** PL spectra of sample-A (ND thickness: 4 nm, diameter: 15 nm), sample-B (ND thickness: 4 nm, diameter: 10 nm) and GaAs-QW (thickness: 4 nm). **b** Calculated and measured ground state transition energy of GaAs-ND. **c** Transient PL profile of GaAs-ND sample

instrumental response curve was 15 ps. From the reference double-QW sample, PL originated from the GaAs bulk and QW of 4 nm were observed at 824 (=1.50 eV) and 758 nm (=1.63 eV), respectively. In addition to this, we observed a weak PL peak from the AlGaAs barrier layer at 636 nm (=1.95 eV). On the other hand, from GaAs nanodisk sample, we could obtain a strong photoemission between GaAs band edge and $Al_{0.3}GaA$ band edge in all of GaAs-ND samples; the peak positions are following; sample-A: 693 nm (=1.79 eV), sample-B: 706 nm (=1.76 eV). Compared with the same thickness GaAs-QW, their emissions wavelengths remarkably blue-shift due to quantum confinement. With the classic envelop-function theory, we solve the one band Schrodinger equations to get the electronic structure. We adopted the finite element method (FEM) to describe our NDs shape, size, and component. The calculation results were shown as the solid line, and PL measurement data were shown as the solid square in Fig. 9.18b. Our calculations reveal that due to classic quantum localization effect, the NDs state gradually decreases with increasing diameters which matches with experimental data very well. We want to mention it that the atomic H-regrowth process removed 1–2 nm (2–4 layers atomics) native oxidation GaAs to shrink the GaAs-ND diameter. If including this 2–4 nm diameter shrink, the above calculation was almost consistent with experimental results. This indicates that the emission form the ND was

corresponding to the ground state transition. As we know, only our group reported this convincible photoluminescence originated from quantum dot fabricated with the plasma-based top-down process.

Then, the carrier lifetime was investigated by the time-resolved PL spectrometry with sample-A at around 693 nm to understand a crystal structure (Fig. 9.18c). Lifetime analysis obtains information about non-radiative relaxation of carriers through defect states. The PL decay profile was fitted by a single-exponential function, and the decay time was 300 ps. The observed PL lifetime of the GaAs-ND is in same order to the values compared with the same thickness GaAs-QW. This lifetime is similar to that of GaAs-QD fabricated by a droplet epitaxy of 150–400 ps [42, 43]. In addition, long lifetime component due to defect-related relaxation process could not be observed in these spectra. These results indicate a satisfactory crystalline structure of our GaAs-NDs. We obtained a strong PL spectrum from the 15 nm diameter GaAs nanodisk structures fabricated using the combination of bio-template technique, NBE, and atomic hydrogen-assisted MBE because of internal defect-free and surface dangling bond-free nanostructures.

9.8 Summary

In this chapter, the novel fabrication processes of Si and GaAs nanodisk arrays by combination of bio-template and neutral beam etching processes were discussed.

The direct formation of a uniform, closely packed, and high density two-dimensional array of ferritin molecules was realized on Si and GaAs substrates using our developed NBO technique to prepare the surface oxide. The neutral beam oxidation process was applied to form both SiO_2 and GaAs oxide thin films that have negative zeta potential and highly hydrophilic surfaces. It was experimentally proven that surface hydrophilicity is essential for the mechanism of uniform and high density ferritin arrangement.

Uniform and defect-free 2D and 3D array of Si-NDs with ND density of more than 7×10^{11} cm^{-2} were realized as Si-QD super lattice structure using combination of bio-templates and NBE processes. The defect-free process with our top-down concept was verified by ESR measurement and PL spectra. The diameter of Si-ND could be controlled by changing the conditions under which surface-oxide removal was conducted.

2D array of GaAs-NDs with ND density of 7×10^{11} cm^{-2} has been developed successfully. Each step of the process, i.e., ferritin protein shell removal, NBE, and iron core removal, has been investigated and several novel solutions have been developed that do not damage the GaAs substrate. O-radicals were first found to eliminate the protein shell effectively at a low temperature of 280 °C without deteriorating surface roughness or moving the iron oxide cores. NBE with a 22 % chlorine and 78 % argon gas mixture and 16 W RF bias power can etch a GaAs nanostructure with a diameter of about 10 nm, atomic-level surface roughness of less than 1 nm and vertical taper angle of 88°.

References

1. S. Baskoutas, A.F. Terzis, Size-dependent band gap of colloidal quantum dots. J. Appl. Phys. **99**, 013708 (2006)
2. H. Yu, J. Li, R.A. Loomis, P.C. Gibbons, L.W. Wang, E.W. Buhro, Cadmium selenide quantum wires and the transition from 3D to 2D confinement. J. Am. Chem. Soc. **125**, 16168 (2003)
3. A. Kongkanand, K. Tvrdy, K. Takechi, M. Kuno, P.V. Kamat, Quantum dot solar cells. Tuning photoresponse through size and shape control of CdSe–TiO_2 architecture. J. Am. Chem. Soc. **130**, 4007 (2008)
4. B. Pejova, I. Grozdanov, Three-dimensional confinement effects in semiconducting zinc selenide quantum dots deposited in thin-film form. Mater. Chem. Phys. **90**, 35 (2005)
5. L. Goldstein, F. Glas, J.Y. Marzin, M.N. Charasse, G. Le Roux, Growth by molecular beam epitaxy and characterization of InAs/GaAs strained-layer superlattice. Appl. Phys. Lett. **47** (10), 1099–1101 (1985)
6. A. Luque, A. Marti, Increasing the efficiency of ideal solar cells by photon induced transitions at intermediate levels. Phys. Rev. Lett. **78**, 5014 (1997)
7. A.A. Konakov, V.A. Burdov, Optical gap of silicon crystallites embedded in various wide-band amorphous matrices: role of environment. J. Phys. Condens. Matter **22**, 215301 (2010)
8. L.H. Thamdrup, F. Persson, H. Bruu, A. Kristensen, H. Flyvbjerg, Experimental investigation of bubble formation during capillary filling of SiO_2 nanoslits. Appl. Phys. Lett. **91**, 163505 (2007)
9. G. Conibeer, M.A. Green, R. Corkish, Y. Cho, E.C. Cho, C.W. Jiang, T. Fangsuwannarak, E. Pink, Y. Huang, T. Puzzer, T. Trupke, B. Richards, A. Shalav, K.L. Lin, Silicon nanostructures for third generation photovoltaic solar cells. Thin Solid Films **511/512**, 654 (2006)
10. E.C. Cho, S. Park, X. Hao, D. Song, G. Conibeer, S.C. Park, M.A. Green, Silicon quantum dot/crystalline silicon solar cells. Nanotechnology **19**, 245201 (2008)
11. Y. Okada, R. Oshima, A. Takata, Characteristics of InAs/GaNAs strain-compensated quantum dot solar cell. J. Appl. Phys. **106**, 024306 (2009)
12. R.B. Laghumavarapu, M. El-Emawy, N. Nuntawong, A. Moscho, L.F. Lester, D.L. Huffakerb, Improved device performance of InAs/GaAs quantum dot solar cells with GaP strain compensation layers. Appl. Phys. Lett. **91**, 243115 (2007)
13. R.P. Raffaelle, S.L. Castro, A.F. Hepp, S.G. Bailey, Quantum dot solar cells. Prog. Photovolt. Res. Appl. **10**, 433 (2002)
14. G. Conibeer, M.A. Green, E.C. Cho, D. König, Y.H. Cho, T. Fangsuwannarak, G. Scardera, E. Pink, Y. Huang, T. Puzzer, S. Huang, D. Song, C. Flynn, S. Park, X. Hao, D. Mansfield, Silicon quantum dot nanostructures for tandem photovoltaic cells. Thin Solid Films **516**, 6748 (2008)
15. X.J. Hao, A.P. Podhorodecki, Y.S. Shen, G. Zatryb, J. Misiewicz, M.A. Green, Effects of Si-rich oxide layer stoichiometry on the structural and optical properties of Si QD/SiO_2 multilayer films. Nanotechnology **20**, 485703 (2009)
16. Y. Kurokawa, S. Tomita, S. Miyajima, A. Yamada, M. Konagai, Photoluminescence from silicon quantum dots in Si quantum dots/amorphous SiC superlattice. Jpn. J. Appl. Phys. **46**, L833 (2007)
17. X. Wen, L.V. Dao, P. Hannaford, Temperature dependence of photoluminescence in silicon quantum dots. J. Phys. D Appl. Phys. **40**, 3573 (2007)
18. I. Yamashita, Fabrication of a two-dimensional array of nano-particles using ferritin molecule. Thin Solid Films **393**, 12 (2001)
19. S. Samukawa, K. Sakamoto, K. Ichiki, Generating high-efficiency neutral beams by using negative ions in an inductively coupled plasma source. J. Vac. Sci. Technol. A **20**, 1566 (2002)

20. S. Samukawa, K. Sakamoto, K. Ichiki, High-efficiency low energy neutral beam generation using negative ions in pulsed plasma. Jpn. J. Appl. Phys. **40**, L997 (2001)
21. S. Samukawa, K. Sakamoto, K. Ichiki, High-efficiency neutral-beam generation by combination of inductively coupled plasma and parallel plate DC bias. Jpn. J. Appl. Phys. **40**, L779 (2001)
22. M. Yonemoto, T. Ikoma, K. Sano, K. Endo, T. Matsukawa, M. Masahara, S. Samukawa, Low temperature, beam-orientation-dependent, lattice-plane-independent, and damage-free oxidation for three-dimensional structure by neutral beam oxidation. Jpn. J. Appl. Phys. **48**, 04C007 (2009)
23. C.H. Huang, M. Igarashi, M. Wone, Y. Uraoka, T. Fuyuki, M. Takeguchi, I. Yamashita, S. Samukawa, Two-dimensional Si-nanodisk array fabricated using bio-nano-process and neutral beam etching for realistic quantum effect devices. Jpn. J. Appl. Phys. **48**, 04C187 (2009)
24. A. Wada, K. Sano, M. Yonemoto, K. Endo, T. Matsukawa, M. Masahara, S. Yamasaki, S. Samukawa, High-performance three-terminal fin field-effect transistors fabricated by a combination of damage-free neutral-beam etching and neutral-beam oxidation. Jpn. J. Appl. Phys. **49**, 04DC17 (2010)
25. S. Samukawa, Ultimate top-down etching processes for future nanoscale devices. Jpn. J. Appl. Phys. **45**, 2395 (2006)
26. M.F. Hochella Jr., A.H. Carim, A reassessment of electron escape depths in silicon and thermally grown silicon dioxide thin films. Surf. Sci. Lett. **197**, 260 (1988)
27. Z.H. Lu, B. Bryskiewicz, J. McCaffrey, Z. Wasilewski, M.J. Graham, Ultraviolet-ozone oxidation of GaAs(100) and InP(100). J. Vac. Sci. Technol. B **11**, 2033 (1993)
28. T. Matsui, N. Matsukawa, K. Iwahori, K. Sano, K. Shiba, I. Yamashita, Realizing a two-dimensional ordered array of ferritin molecules directly on a solid surface utilizing carbonaceous material affinity peptides. Langmuir **23**, 1615 (2007)
29. T. Matsui, N. Matsukawa, K. Iwahori, K. Sano, K. Shiba, I. Yamashita, Direct production of a two-dimensional ordered array of ferritin-nanoparticles on a silicon substrate. Jpn. J. Appl. Phys. **46**, L713 (2007)
30. H. Nishino, N. Hayasaka, H. Okano, Damage-free selective etching of Si native oxides using NH_3/NF_3 and SF_6/H_2O down-flow etching. J. Appl. Phys. **74**, 1345 (1993)
31. J. Kikuchi, M. Iga, H. Ogawa, S. Fujimura, H. Yano, Native oxide removal on Si surfaces by NF_3-added hydrogen and water vapor plasma downstream treatment. Jpn. J. Appl. Phys. Part 1 **33**, 2207 (1994)
32. L. Pavesi, L.D. Negro, C. Mazzoleni, G. Franzo, F. Priolo, Optical gain in silicon nanocrystals. Nature **408**, 440 (2000)
33. K. Kůsová, O. Cibulka, K. Dohnalova, I. Pelant, J. Valenta, A. Fučíková, K. Zıdek, J. Lang, J. Englich, P. Matějka, P. Štěpánek, S. Bakardjieva, Brightly luminescent organically capped silicon nanocrystals fabricated at room temperature and atmospheric pressure. ACS Nano **4**(8), 4495 (2010)
34. W. Boera, H. Zhangb, T. Gregorkiewicz, Optical spectroscopy of carrier relaxation processes in Si nanocrystals. Mater. Sci. Eng. B **159–160**, 190 (2003)
35. I.A. Walmsley, Looking to the future of quantum optics. Science **29**, 1211 (2008)
36. X.Y. Wang, C.H. Huang, Y. Ohno, M. Igarashi, A. Murayama, S. Samukawa, Defect-free etching process for GaAs/AlGaAs heteronanostructure using chlorine/argon mixed neutral beam. J. Vac. Sci. Technol. B **28**, 1138 (2010)
37. T. Yoshikawa, Y. Sugimoto, S. Kohmoto, S. Kitamura, K. Makita, Y. Nambu, K. Asakasa, Dry etching and consequent burring regrowth of nanosize quantum wells stripes using an in situ ultrahigh vacuum multichamber system. J. Vac. Sci. Technol. B **16**, 1 (1998)
38. X.Y. Wang, Y. Ohno, M. Igarashi, M. Murayama, S. Samukawa, Damage-free top-down processes for fabricating two-dimensional arrays of 7 nm GaAs nanodiscs using biotemplates and neutral beam etching. J. Vac. Sci. Technol. B **28**, 1138 (2010)

39. X.Y. Wang, C.H. Huang, R. Tsukamoto, P.A. Mortemousque, K.M. Itoh, Y. Ohno, S. Samukawa, Damage-free top-down processes for fabricating two-dimensional arrays of 7 nm GaAs nanodiscs using bio-templates and neutral beam etching. Nanotechnology **22**, 365301 (2011)
40. M. Igarashi, R. Tsukamoto, C.H. Huang, I. Yamashita, S. Samukawa, Direct fabrication of uniform and high density sub-10-nm etching mask using ferritin molecules on Si and GaAs surface for actual quantum-dot superlattice. Appl. Phys. Expres. **4**, 015202 (2011)
41. R. Tsukamoto, M. Muraoka, Y. Fukushige, H. Nakazawa, T. Kawaguchi, Y. Nakatsuji, I. Yamashita, Improvement of Co_3O_4 nanoparticle synthesis in apoferritin cavity by outer surface PEGylation. Bull. Chem. Soc. Jpn **81**, 1669 (2008)
42. Y. Tamura, T. Kaizu, T. Kiba, M. Igarashi, R. Tsukamoto, A. Higo, W. Hu, C. Thomas, M. E. Fauzi, T. Hoshii, I. Yamashita, Y. Okada, A. Murayama, S. Samukawa, Quantum size effects in GaAs nanodisks fabricated using a combination of the bio-template technique and neutral beam etching, Nanotechnology **24**, 285301 (2013)
43. I. Yamashita, A. Murayama, S. Samukawa, Light-emitting devices based on top-down fabricated GaAs quantum nanodisks. Scientific Reports **5**, 9371 (2015)